Investigation of cerium as a surrogate for tetravalent actinides in monazite-type compounds

Theresa Lender [a,*], Elena Bazarkina [b,c], Kristina O. Kvashnina [b,c], Nina Huittinen [b,d], Lars Peters [a]

[a] *Institute of Crystallography, RWTH Aachen University, Jägerstraße 17-19, Aachen, 52066, Germany*
[b] *Institute of Resource Ecology, Helmholtz-Zentrum Dresden-Rossendorf, Bautzner Landstraße 400, Dresden, 01328, Germany*
[c] *The Rossendorf Beamline at ESRF, The European Synchrotron, 71 Avenue des Martyrs, Grenoble, 38043, France*
[d] *Institute of Chemistry and Biochemistry, Freie Universität Berlin, Fabeckstraße 34-36, Berlin, 14195, Germany*

ARTICLE INFO

ABSTRACT

The incorporation of tetravalent cerium into the monazite structure *via* Ca(II)-coupled substitution was investigated using a solid state and a co-precipitation route for the synthesis of the $La_{1-2x}Ca_xCe_xPO_4$ solid solution. Based on powder XRD measurements and elemental mappings an optimised synthesis procedure was developed that averts the formation of secondary phases and allows the stabilisation of tetravalent cerium with a ratio of up to 0.21 Ce(IV)/Ce(III). *In-situ* HERFD-XANES measurements at the Ce L_3 edge at up to 800 °C were performed to study the cerium oxidation state during the phase transformation from rhabdophane to monazite, revealing an unexpected non-linear behaviour as well as a charge-directing effect of the lanthanum cation.

1. Introduction

As of 31. December 2022, 408 nuclear power reactors were operated in 32 countries with an additional 58 reactors in 18 countries under construction [1]. Developing suitable strategies for safe and sustainable storage of radioactive wastes thus becomes an increasingly pressing challenge. The incorporation of high-level waste (HLW) into inorganic solids like glasses, ceramics, or composite materials has long been investigated to ensure long-term immobilisation of radionuclides [2].

Many countries like France, the UK, the USA, India, Japan, Belgium, Germany, and Russia have used vitrification, the process of dissolving radioactive waste in a glassy host matrix, for decades [3–5]. This method is attractive mainly because the production of waste-loaded glass is simple and a wide variety of elements can be immobilised in the amorphous structures. Borosilicate glasses exhibit a high thermal and chemical durability as well as tolerance to radiation damage [6,7]. Drawbacks of this method are the low solubility of some radionuclides like actinides in glass, resulting in moderate waste loading capacities [5,7] and increased leaching rates of HLW glasses in acidic media [8].

The idea of immobilising radionuclides in crystalline phases was first put forward by Hatch in 1953 [9]. Since then, continuous research has been conducted on a wide variety of crystalline host matrixes. This includes single-phase ceramics like monazite, zirconia, pyrochlore and perovskite [10] and polyphase ceramics, most notably Synroc [5]. A common advantage of crystalline phases compared to amorphous host phases is a higher waste loading and better retention capacity due to the incorporation of radionuclides at specific atomic positions of the crystal structures [5].

Monazite has long been considered as one of the most promising crystalline host materials for long-term storage of radioactive waste, especially actinides. As a major thorium source, natural monazite ores can contain more than 20 wt% ThO_2 [11,12] and up to 16 wt% UO_2 [13, 14]. Special attention has been drawn to this mineral by the absence of metamict specimens irrespective of high self-irradiation doses indicating an exceptional resistance against radiation damage [15]. This is generally ascribed to the extraordinarily low annealing temperature of rare earth orthophosphates ($REEPO_4$ with REE = rare earth elements Sc, Y, lanthanides La-Lu) with the critical amorphisation temperature T_C of $LaPO_4$ being as low as 60 °C [10,16]. Additionally, a repair mechanism based on annealing induced by alpha particles has been described, resulting in moderate levels of radiation damage in natural samples irrespective of the total irradiation dose [15]. Structurally, monazite consists of PO_4 tetrahedra and LnO_9 polyhedra that are alternately connected to form chains in the [001] direction (see Fig. 1). Four of the nine oxygen atoms of the LnO_9 polyhedra form bonds with the neighbouring PO_4 tetrahedra while the remaining five oxygen atoms,
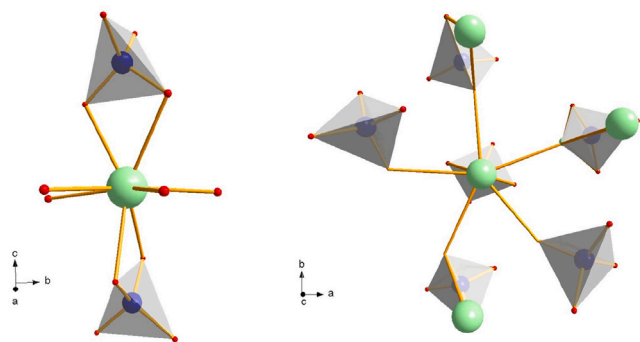

Fig. 1. Left: Structural model of a LnO_9 polyhedron connected to two PO_4 tetrahedra in the [001] direction. Right: The five oxygen atoms in the equatorial plane form connections to neighbouring chains resulting in the locking effect.

located in the equatorial plane of the polyhedra, form connections with five surrounding chains resulting in the so-called *locking effect* [17,18]. The irregular nine-fold coordination of the lanthanide cations does not impose severe restrictions on the size and charge of the cation resulting in a high chemical flexibility of this position.

The ability of the monazite structure to retain trivalent actinides or lanthanides – acting as inactive surrogates – has been comprehensively documented [14,19–30]. Several publications also report on the successful incorporation of tetravalent actinides *via* coupled substitution mechanisms, namely thorium, uranium, and neptunium [14, 31–34]. However, the synthesis of pure $M(II)_{0.5}Pu_{0.5}PO_4$ as well as $M(II)_{0.5}Ce_{0.5}PO_4$ (M = Mg, Ca, Sr, Ba and Cd) containing cerium as an inactive surrogate of plutonium is deemed impossible due to the reduction of both Pu(IV) and Ce(IV) to the trivalent state [35,36]. Bregiroux et al. [37] achieved a partial inclusion of tetravalent plutonium resulting in a compound with the formula $Pu_{0.4}^{(III)}Pu_{0.3}^{(IV)}Ca_{0.3}^{(II)}PO_4$ while $Pu^{(III)}PO_4$ was synthesised from a $Pu^{(IV)}O_2-NH_4H_2PO_4$ mixture under argon atmosphere. Though Orlova et al. [38] claim the successful synthesis of $BaCe(PO_4)_2$, Popa et al. [36] argue that cerium is reduced to form $CePO_4$ while barium is probably contained in an amorphous phase visible in the XRD diffractogram of their synthesis product. Similarly, Kitaev et al. [39] observe reflections of an impurity phase when attempting to synthesise $SrCe(PO_4)_2$ and $BaCe(PO_4)_2$. Doubts may be raised about the tetravalent state of cerium in these compositions as the oxidation state was not determined in this work.

Lanthanides are often used as surrogates for actinides as they show a similar chemical behaviour due to a high degree of similarity in atomic radii and electronic configuration. Of the suitable lanthanides, only cerium exhibits a stable tetravalent state under atmospheric conditions as well as a similar redox potential as Pu(IV)/Pu(III) and U(V)/U(IV), thus making it the most promising surrogate [40,41]. Due to the variable valency +3/+4 observed in both elements as well as the excellent correspondence of the ionic radii [42–44], cerium is commonly used as a surrogate especially for plutonium. In this work, the suitability of cerium as a surrogate for tetravalent actinides will be examined based on the crystal structure of cerium-doped monazite powders prepared by both, dry and wet chemical routes. While solid state synthesis of monazites is the most established method, wet chemical routes are preferable in a controlled area due to reduced dust formation and increased homogeneity of the final product.

2. Materials and methods

The solid solution $La_{1-2x}Ca_xCe_xPO_4$ (x = 0-0.5 with Δx = 0.05) was prepared by both a solid state and a co-precipitation route. The products were studied by a range of analytical methods.

2.1. Synthesis methods

The solid state synthesis of monazites from the respective oxides has already been described in literature [35]. An excess of 10 wt% $NH_4H_2PO_4$ was added to the metal oxides to prevent the formation of phosphate-deficient phases. After grinding the starting materials, pellets were pressed to increase grain contact. The calcination was performed at 1250 °C for 24 h.

The procedure of the co-precipitation route *via* rhabdophane is described in detail by Heuser et al. [45]. $La(NO_3)_3$, $Ca(NO_3)_2$ and $(NH_4)_2Ce(NO_3)_6$ were mixed with an excess of phosphoric acid (La:P = 1:5) and citric acid, which was used as a complexing agent. Precipitation of rhabdophane was induced by increasing the pH with 12.5% ammonia solution. The precipitate was washed six times with ultrapure water. After drying, the powders were thermally treated at 550 °C for 3 h and at 800 °C for 24 h to remove crystal water and obtain monazite. For the sake of comparability with the samples obtained *via* the solid state route, a fraction of all obtained powders was also submitted to heat treatment at 1250 °C.

2.2. Analytical methods

X-ray diffraction patterns were obtained using a Bruker AXS D8 Advance diffractometer equipped with a Cu-tube and a Ni-filter at a tube voltage of 40 kV and a current of 40 mA. The measurements were performed with a LynxEye detector at ambient temperatures in the 2 θ-range of 15-140° with a step size of 0.0105° and increasing counting times to enhance signal quality in the high angle range (15-50°: 0.8 s/step, 50-100°: 1.7 s/step, 100-140°: 3.5 s/step). Structure refinements were performed using the Rietveld-method [46] with a fundamental parameters approach within the *Topas Academic* software (Version 7.21; Cheary and Coelho [47]). During the refinements, a ten coefficient Chebyshev-polynomial was used to describe the background. Crystallite size, lattice parameters and fractional coordinates of all sites were allowed to vary. Individual scaling factors were introduced for all ranges. To account for the lower scattering power of oxygen and phosphorous compared to lanthanides, soft distance restraints for the P–O bonds were implemented at a value of 1.52 Å. The $LaPO_4$ structure published by Hirsch et al. [48] was used as starting model for the structural refinement. It should be noted that the estimated standard deviations of refined parameters are systematically underestimated in Rietveld refinements due to local correlations [49,50]. Raw data and Rietveld refinements are available online [51].

DSC/TGA measurements were performed in a *STA 449 F3 Jupiter* thermal analyser under synthetic air. PtRh20 crucibles were used as sample containers.

Electron probe micro analysis (EPMA) was performed with a *Jeol Superprobe JXA-8900R*, equipped with 5 WD/ED combined microanalysers. Synthetic *REE* orthophosphates, provided by the Smithsonian Institution [52], corrected for their Pb content according to Donovan et al. [53], were used as standards for P and *REE*. Measurements were carried out with an acceleration voltage of 20 kV, a probe current of 40 nA and a focused beam size of 1 μm diameter. Counting times were set to 20 s with two background measurements of 10 s duration.

TEM measurements were performed on a *JEOL JEM F200* with an acceleration voltage of 200 kV. The preparation of FIB lamellae was performed with a *FEI Strata 400* using a Ga Liquid Metal Ion Source.

The high-energy resolution fluorescence detection (HERFD) X-ray absorption near edge structure (XANES) spectra at the Ce L_3 edge were recorded at the Rossendorf Beamline BM20 [54] of the European Synchrotron Radiation Facility (ESRF) in Grenoble, France. The storage ring was operated at 6 GeV with a ≈ 200 mA current in 7/8+1 filling mode. The incident photon energies were selected using a double Si(111) crystal monochromator, higher harmonics were suppressed by two Si mirrors operating in total reflection mode. The vertically focused beam size was 50 × 2000 μm². The incident energy was calibrated using
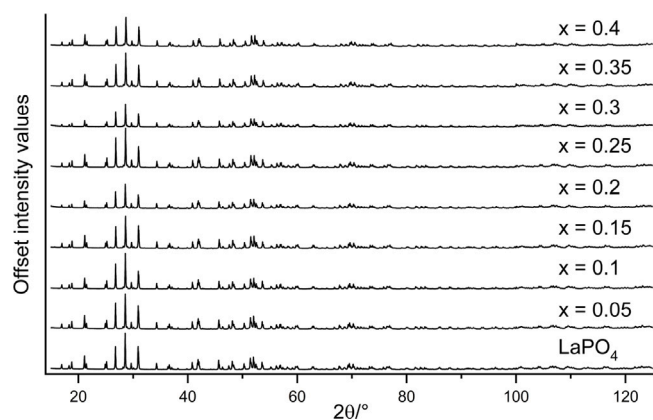
Fig. 2. Powder diffractograms of the $La_{1-2x}Ca_xCe_xPO_4$ solid solution produced by solid state synthesis. No evidence of an impurity phase was observed.

a standard crystalline powder of CeO_2 pressed into a pellet; the Ce L_3 edge energy position was set to 5723.2 eV as the maximum of the first derivative of the main-edge HERFD-XANES spectrum. All synthetic samples and reference compounds were pressed into pellets, placed vertically, rotated by 45° to the incident beam and analysed under ambient conditions. *In-situ* HERFD-XANES measurements were performed in a furnace developed at the ESRF. Photographs of the set-up are provided in the SI (Figure S5). A Johann-type X-ray emission spectrometer in a vertical Rowland geometry available at BM20 [55] was equipped with spherically bent crystal Ge(331) analysers with a 1 m bending radius, and a silicon drift X-ray detector (© Ketek). For HERFD measurements at Ce L_3 edge (5723 eV), the spectrometer was aligned at the maximum of the Ce $L\alpha 1$ emission line (4839.2 eV) using the (331) reflection and the 80.8° Bragg angle. HERFD-XANES measurements were performed in the energy range 5710–5779 eV with a typical acquisition time of 4 min per spectrum. The pre-edge region (5710–5722 eV) was additionally analysed with increased counting times resulting in an acquisition time of 2 min per spectrum. All spectra were normalised using the Athena software [56] and analysed with the help of the iterative transformation factor analysis (ITFA; Rossberg et al. [57]). The raw data is available online [58] and a short explanation of the ITFA procedure is provided in the SI.

3. Results and discussion

3.1. Solid state synthesis

Samples with the nominal compositions of the solid solution $La_{1-2x}Ca_xCe_xPO_4$ ($\Delta x = 0.05$) were synthesised with the solid state method up to $x = 0.4$. The two missing compositions $La_{0.1}Ca_{0.45}Ce_{0.45}PO_4$ and $Ca_{0.5}Ce_{0.5}PO_4$ could not be produced with this method, since the pellets melted during the heat treatment and the resulting material could not be removed from the crucibles. XRD measurements indicate phase purity of all synthesised samples as shown in Fig. 2. Due to the use of restraints for the P-O distances in the Rietveld refinement as described in the previous section, the evaluation of bond lengths and angles is not meaningful.

Similar to Bregiroux et al. [59], we used both, electronic microprobe measurements, and XRD to investigate the oxidation state of cerium in the monazite samples. A first estimation was made based on the reported linear relationship between the unit cell parameters of monazite and the cation size [60]. By comparison of the measured lattice parameters to the known behaviour of monazite solid solutions, conclusions can be drawn about the success of the calcium incorporation needed for charge balancing. Since the true average effective cationic radii in the solid solutions are unknown, two different models were calculated and

compared to literature data, to account for two substantially different substitution mechanisms. The first model assumes that lanthanum is replaced by stoichiometric amounts of tetravalent cerium and divalent calcium, reflecting a "classical" coupled substitution-behaviour as described in the following equation for the solid state reaction:

$$(1 - 2x)La_2O_3 + 2xCeO_2 + 2xCaO + 2NH_4H_2PO_4$$

$$\rightarrow 2La_{1-2x}Ce(IV)_xCa_xPO_4 + 2NH_3 + 3H_2O \qquad (1)$$
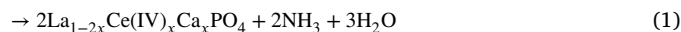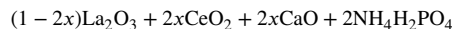
Consequently, the average ionic radius is determined by:

$$R_{average} = (1 - 2x)R_{La(III)}^{IX} + xR_{Ce(IV)}^{IX} + xR_{Ca(II)}^{IX} \qquad (2)$$

In the second model, we assumed a quantitative reduction of cerium to its trivalent state and corresponding quantitative incorporation, without any incorporation of divalent calcium in the monazite-type phase. This scenario can be described as:

$$(1 - x)La_2O_3 + 2xCeO_2 + 2NH_4H_2PO_4$$

$$\rightarrow 2La_{1-x}Ce(III)_xPO_4 + 2NH_3 + 3H_2O + x/2O_2 \qquad (3)$$
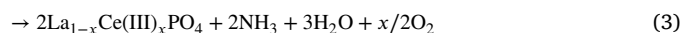
with the average ionic radius in the monazite structure being:

$$R_{average} = (1 - x)R_{La(III)}^{IX} + xR_{Ce(III)}^{IX} \qquad (4)$$

As shown in Fig. 3 there is a strong deviation between model 1 (left) and the literature data, with the change in lattice parameters being significantly smaller than expected for a corresponding effective ionic radius in the monazite structure. On the other hand, model 2 displayed on the right in Fig. 3 is highly consistent with the literature data. Based on this comparison, a substitution mechanism reflected in the second model seems more probable.

These conclusions are consistent with conclusions drawn by Bregiroux et al. [59] with regards to $La_{1-2x}Ca_xCe_xPO_4$ and by Bregiroux et al. [37] with regards to $CaPu(PO_4)_2$, stating that only incomplete incorporation of tetravalent cerium and plutonium is possible and that the excess calcium forms a secondary phase.

The results obtained by electron probe microanalysis are shown in Fig. 4. Electron imaging reveals two clearly distinct phases based on the average atomic number: A high-contrast phase that contains heavy ions forming regular crystallites, while the cavities are occupied by a phase with low contrast that shows no detectable preference for a specific shape. The elemental mappings reveal that the high-contrast phase contains lanthanum and cerium, while calcium can be found in the low-contrast areas.

Based on this information, it can be concluded that cerium is reduced during sintering at 1250 °C and incorporated into the monazite structure in a trivalent state while calcium forms a secondary phosphate phase.

According to electron diffraction of the calcium-rich intergranular areas of solid state powders, this secondary phase is highly crystalline (see Fig. 5). Bregiroux et al. [59] observed the formation of $Ca_2P_2O_7$ in their samples. The presence of significant amounts of calcium pyrophosphate ($T_m = 1230$ °C) would explain the melting observed in the two compositions with the highest Ca content. It can be difficult to detect in a diffractogram since high intensity peaks of $Ca_2P_2O_7$ are superimposed by monazite reflections [37] and the scattering power of calcium is considerably lower than that of lanthanum and cerium. Still, it is surprising that systematically no signs of a secondary phase were observed in the powder diffractograms.

3.2. Co-precipitation synthesis

Using the co-precipitation method, it was possible to produce powders spanning the whole range of the solid solution, all showing Bragg reflections associated with a monazite-type structure. The low incorporation capacity of the rhabdophane structure for actinides reported
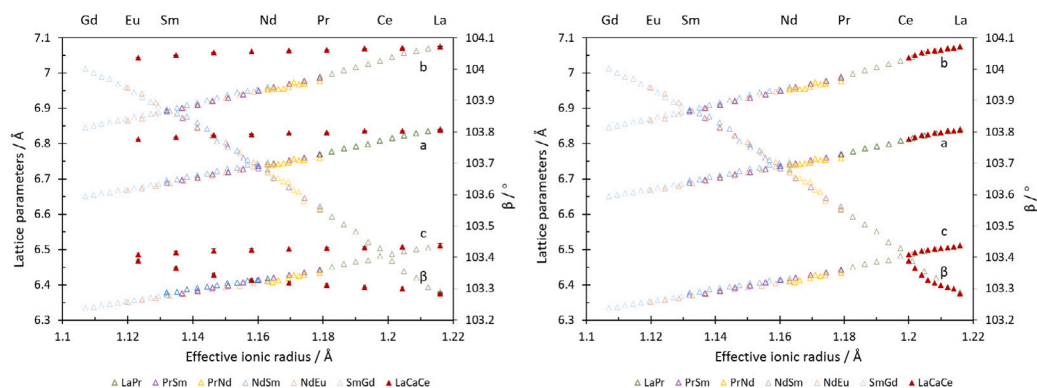
Fig. 3. Comparison of lattice parameters of solid state samples based on two substitution models with literature data from lanthanide solid solutions [60]. Left: Incorporation of tetravalent cerium and calcium for charge balance. Right: Incorporation of trivalent cerium. Error bars are smaller than symbols.
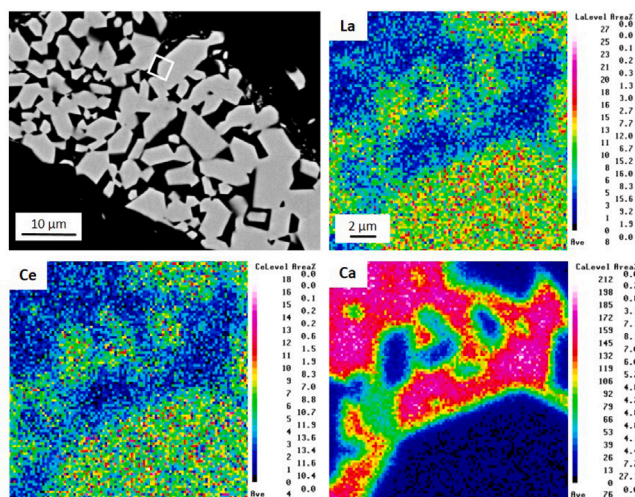

Fig. 4. Top left: Electron backscattering image of a powder sample synthesised *via* a solid state reaction. The mapping area is indicated by the white square in the backscattering image. Top right to bottom right: Elemental mappings of lanthanum, cerium and calcium show the corner of a monazite crystallite surrounded by a calcium-rich phase.
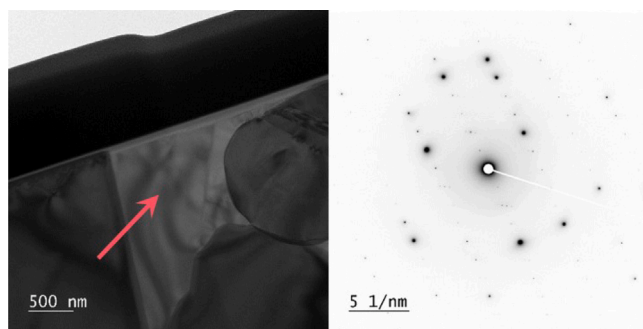

Fig. 5. Electron diffraction pattern from TEM lamella (arrow indicates analysed spot) shows high degree of crystallinity of Ca-rich phase.

in literature (e.g. $x_{Th} \leq 0.15$ according to Qin et al. [61], Zhao et al. [62]) did not inhibit this synthesis, as rhabdophane was only formed in a protocrystalline state. This seems to allow the incorporation of cations that would not be accommodated in the fully crystalline structure. In fact, we were able to synthesise two full monazite-cheralite solid solutions with the same synthesis procedure, reaching $x_{Th} = 0.5$ [63].

As indicated in Fig. 6, some small additional features are observed in several compositions sintered at 1250 °C indicating the presence of

an impurity phase. Compositions with calcium insertion rates $x_{Ca} < 0.3$ contain α-Ca$_2$P$_2$O$_7$ as a secondary phase while a mixture of α-Ca$_2$P$_2$O$_7$ and β-Ca$_3$P$_2$O$_8$ was observed in powders with $0.3 \leq x_{Ca} < 0.4$. Increasing the insertion rate up to the maximum of $x_{Ca} = 0.5$ results in β-Ca$_3$P$_2$O$_8$ being the only secondary phase. This observed increase in the Ca:P ratio correlates with the increasing amount of calcium segregating from the monazite phase.

No impurities were detected in powders heated only to 800 °C. This temperature was chosen on the basis of DSC measurements which showed that the phase change from rhabdophane to monazite occurred between 600 °C and 800 °C depending on the cerium content (see Figure S2 in the SI). This corresponds well to findings from Matraszek et al. [64] and Mesbah et al. [65]. To minimise the reduction of cerium while still ensuring a rapid and complete reaction, the temperature of 800 °C was chosen. The reflections observed in the diffractograms of these powders are very broad, as shown in Figure S1 in the SI. This phenomenon has been attributed to the low degree of crystallinity of the monazite phase after dehydration [66]. In fact, high resolution TEM images show that these powders are only partly crystalline (see Fig. 7). The *Fourier*-transform of the crystalline areas could be indexed with the monazite structure in agreement with the PXRD measurements. This may indicate that the addition of calcium impedes the phase conversion of rhabdophane to monazite, which is known to occur rapidly at 800 °C for undoped samples [67].

As shown in Fig. 8, the electron backscattering images of the co-precipitated samples vary considerably depending on the calcination temperature. In powders that were subjected to 1250 °C, the crystallites consist of the phase of high electron density with inclusions of low electron density (see Fig. 8 a). Again, lanthanum and cerium were detected in the high-contrast areas while calcium could only be found in the low-contrast inclusions. In comparison, a wide variety of different contrasts can be found in the precipitated powders treated at 800 °C. Here, no segregation of the cations is observed, as shown in the elemental mappings in Fig. 8(b). Separate EDX measurements confirmed this finding (see Figure S3 in the SI). The variability in contrast is likely a result of variable particle density. Orientation contrast was ruled out based on a tilt series measured with SEM that showed no corresponding changes (see Figure S4 in the SI).

The investigation of the oxidation state of cerium in the co-precipitated samples was performed *via* HERFD-XANES pre-edge analysis [68]. As shown in Fig. 9(a), trivalent and tetravalent cerium show a clearly distinct behaviour. Differences in the pre-edge region highlighted in Fig. 9(b) which corresponds to 2p-4f transitions arise from the varying ground state electron configuration: Ce(IV) has no 4f electrons and Ce(III) has one. Based on this difference, the ratio of tetravalent to trivalent cerium can be quantified using Principal Component Analysis.

Even though the conditions for balancing the charge of tetravalent cerium were given due to successful incorporation of calcium at 800 °C, the ratios of Ce(IV) to Ce(III) were surprisingly low, with a maximum
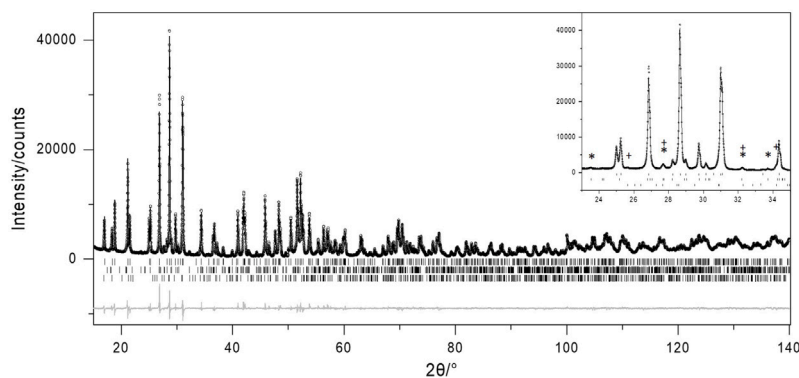
Fig. 6. Powder diffractogram of monazite containing 40% lanthanum, 30% cerium and 30% calcium on the central site produced *via* co-precipitation synthesis and sintering at 1250 °C. Measured intensities are depicted as circles, the fit is given as a line. In grey the difference curve is shown. Tick marks correspond to monazite, α-$Ca_2P_2O_7$ and β-$Ca_3P_2O_8$ from top to bottom. In the inset, reflections of the impurity phases are marked with * for α-$Ca_2P_2O_7$ and + for β-$Ca_3P_2O_7$.

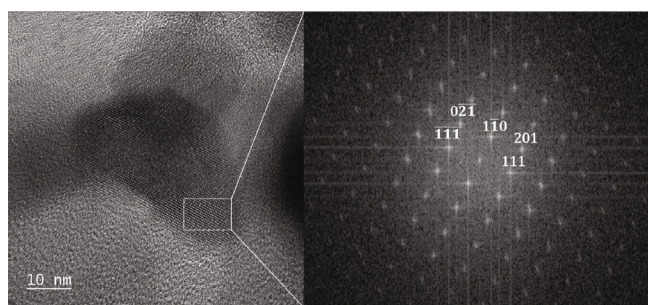**Fig. 7.** High resolution TEM (HRTEM) image of a precipitated crystallite with the target composition $Ca_{0.5}Ce_{0.5}PO_4$. The *Fourier*-transform of the marked area shown on the right can be indexed with a monazite-type cell.

of 0.21 ± 0.02 for $Ca_{0.5}Ce_{0.5}PO_4$. This is only slightly higher than the maximal ratio of 0.15 Bregiroux et al. [59] were able to reach with a solid state method.

For the sake of comparability, the Ce(IV)/Ce(III) ratio was also determined as described by Bregiroux et al. [59] from the lattice parameters determined from XRD analysis. The average ionic radius was estimated from the known linear relationships between the lattice parameters and the ionic radius in monazite solid solutions containing trivalent lanthanides. The resulting values are shown in Fig. 10(a) in comparison to the radii determined by Bregiroux et al. [59] and the pure solid solutions containing only trivalent or tetravalent cerium. Using formula (10) in Bregiroux et al. [59] the Ce(IV)/Ce(III) ratio was determined for all members of the solid solution, as shown in Fig. 10(b). This approach results in significantly higher Ce(IV) levels than determined *via* XANES. Additionally, the trend is reversed, with the highest Ce(IV) level observed in the sample with the lowest loading, contradicting the XANES analysis. A possible explanation for this discrepancy is the assumption that Ce(IV) and Ca occupy the same atomic position in the monazite structure, which is fundamental to this approach. This assumption may not be valid, as it has been shown that Th(IV) and Ca are displaced from the central position of the LnO_9 polyhedron in the cheralite structure [63,69]. The same might be true for Ce(IV) but high quality single crystal XRD data or neutron data would be necessary to confirm this.

To gain a deeper understanding of the redox behaviour of cerium during the sintering procedure, *in-situ* HERFD-XANES measurements were performed at temperatures up to 800 °C. High temperature XANES measurements of the Ce L_3 edge are not uncommon in the area of catalysis (e.g. Gasperi et al. [70], Piskorska-Hommel et al. [71], Morgan et al. [72]) but they are not frequently performed in the field of waste form research and have to our knowledge never been carried
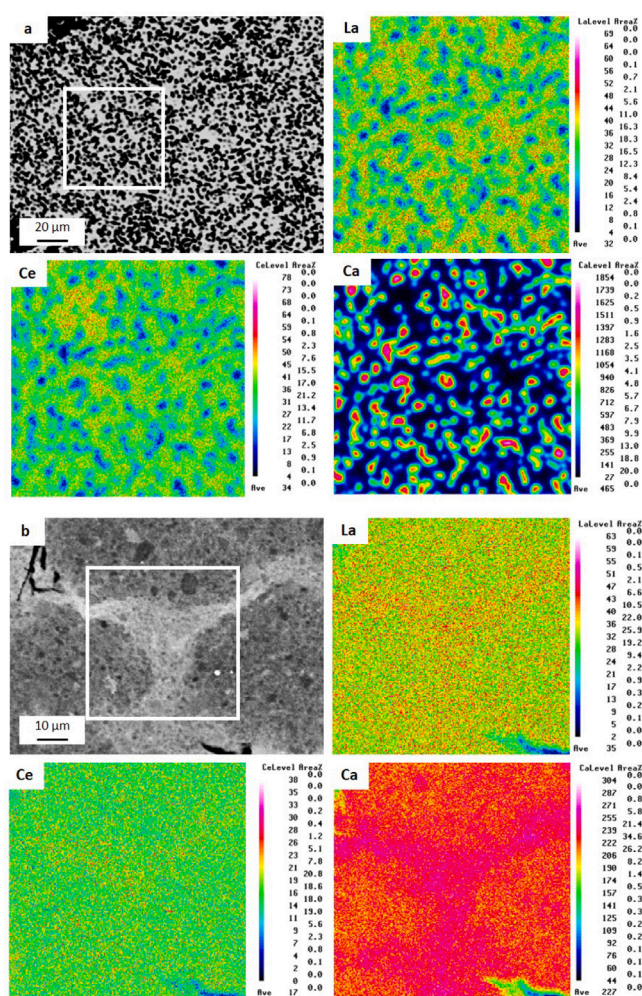

Fig. 8. (a) Electron backscattering image of a powder sample synthesised via co-precipitation and calcined at 1250 °C indicating the mapping area for EDX analysis (white square). Elemental mappings of lanthanum, cerium and calcium show calcium-rich inclusions in a monazite matrix. (b) Electron backscattering image of a sample calcined at 800 °C with the mapping area shown and elemental mappings of lanthanum, cerium and calcium with no observable segregation of the cations.

out on monazites. *In-situ* measurements were performed starting with rhabdophane dried at 50 °C in a custom-made setup at the ESRF (see Fig. 2 in the SI). Fig. 11 shows the changes observed during the heating of $Ca_{0.5}Ce_{0.5}PO_4$ in the full energy range (top left), with variations
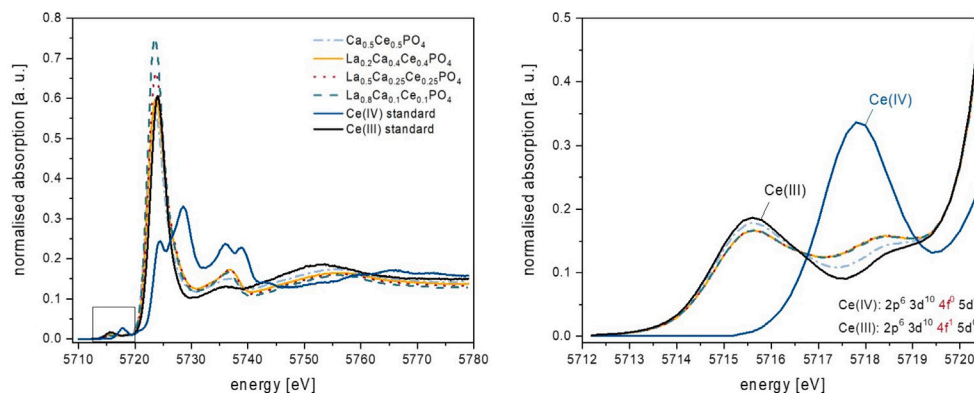
Fig. 9. (a) Ce L$_3$ edge HERFD measurements of monazites with various levels of cerium insertion indicating the predominance of Ce(III). Measurements were performed at ambient temperature after heat treatment at 800 °C. (b) The Ce L$_3$ pre-edge region showing the 2p to 4f electronic transition was used for the quantification of the oxidation states. The Ce(IV)/Ce(III) ratio was found to be 0.21 in Ca$_{0.5}$Ce$_{0.5}$PO$_4$ and approx. 0.07 in the all other samples. The experimental uncertainty is estimated to be 0.02.
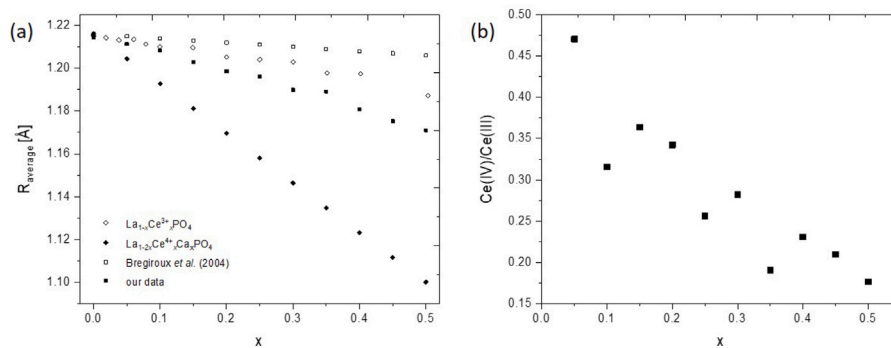

Fig. 10. (a) Average cationic radius versus cerium insertion rate x of co-precipitated samples estimated from lattice parameters. (b) Ce(IV)/Ce(III) ratio of co-precipitated samples determined from XRD data assuming identical atomic position of all cations.

in the 2p to 5d transitions clearly visible, as well as in the pre-edge region (top right), which depicts the 2p to 4f transitions. Changes in the oxidation state of cerium are clearly visible during the first runs after which a stable state seems to be reached. Surprisingly, already the as-precipitated samples mostly contain Ce(III), indicating that the reduction of cerium takes place in solution or during the precipitation process. Thus, lowering the sintering temperature is not necessarily a promising strategy to increase the amount of Ce(IV) incorporated into the structure. The lower panels of Fig. 11 depict the change in Ce(IV)/Ce(III) ratio measured during heating for four different compositions as modelled by the linear combination fits of the pre-edge features using the spectra of CeO$_2$ and CePO$_4$ as standards. In all samples the tetravalent fraction decreases upon heating followed by an oxidation step. As this trend is observed in all samples it can be considered to be significant, even though the absolute changes of the intermediate compositions are within the experimental error range. The temperature at which the oxidation of cerium starts depends on the cerium content, *i.e.* it increases from 350 °C in Ca$_{0.5}$Ce$_{0.5}$PO$_4$ to 750 °C in La$_{0.8}$Ca$_{0.1}$Ce$_{0.1}$PO$_4$. The oxidation seems to be limited with a Ce(IV)/Ce(III) ratio of approximately 0.08 for all samples, except for cheralite, which contains significantly higher levels of tetravalent Ce. This might indicate that the presence of trivalent lanthanum inhibits the incorporation of tetravalent cerium.

This Ce behaviour is unusual and requires further substantial investigation. The most straight-forward explanation for the initial reduction is the relative instability of the tetravalent oxidation state of cerium as indicated by the standard reduction potential of 1.443 V of the reaction Ce(IV) + e$^-$ ⇌ Ce(III) [73]. Another possibility is the presence of a secondary, amorphous phase containing tetravalent cerium that

degrades during the calcination process. Despite extensive washing of the samples, the presence of small amounts of unreacted ceric ammonium nitrate cannot be excluded, either. At higher temperatures, reactions with atmospheric oxygen may stabilise cerium in a tetravalent form. This seems to be limited, as extended holding periods lead to a stagnation of the Ce(IV) to Ce(III) ratio (compare Ca$_{0.5}$Ce$_{0.5}$PO$_4$ in Fig. 11).

4. Conclusion

In this study, we have made significant progress in understanding the challenges posed by the (coupled) substitution of tetravalent cerium into the monazite structure given its unexpected redox behaviour during the synthesis procedure. For the first time, *in-situ* XANES measurements were performed to study the oxidation state of cerium during the sintering process, revealing both, a non-linear behaviour of the cerium oxidation state, and the role of lanthanum stabilising cerium in the trivalent state. In the lanthanum-free end member Ca$_{0.5}$Ce$_{0.5}$PO$_4$, we were able to incorporate tetravalent cerium with a ratio of up to 0.21 Ce(IV)/Ce(III) using the co-precipitation method as evidenced by the *ex-situ* XANES measurements. Higher ratios may be achievable in a more oxidising aqueous environment, as the reduction most probably already occurs in the solution or during the precipitation process. The solid state method is not applicable for the incorporation of tetravalent cerium.

While cerium has only limited value as a surrogate for thorium and uranium, as these show a different redox behaviour, studies on plutonium lead to comparable results with Pu(IV) being reduced to Pu(III) during incorporation into the monazite structure and coupled
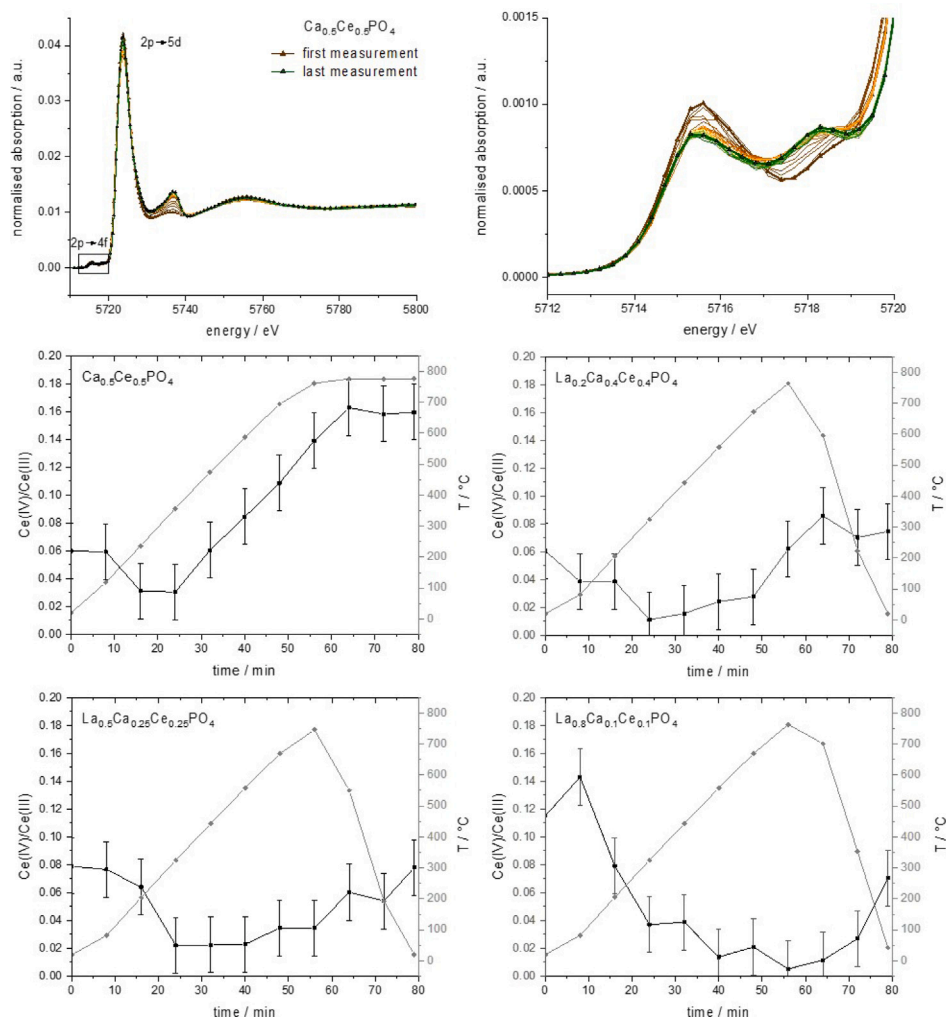
Fig. 11. Top: Full energy spectrum and pre-edge region of the Ce L_3 edge of $Ca_{0.5}Ce_{0.5}PO_4$ during sintering. Bottom: Evolution of the Ce(IV) to Ce(III) ratio in Ce-containing monazite samples. Ceramic pellets were heated to 800 °C with a heating rate of 15 °C/min. Errors are estimated to be within 0.02.

substitution being limited to an insertion rate of 30 % [31,37,74]. This suggests, that initial tetravalent plutonium, just like cerium, may not require any charge compensation for insertion into monazite, especially *via* the co-precipitation method, thereby facilitating the incorporation dramatically.

CRediT authorship contribution statement

Theresa Lender: Writing – original draft, Visualization, Resources, Methodology, Investigation, Data curation, Conceptualization. **Elena Bazarkina:** Writing – review & editing, Validation, Methodology, Investigation. **Kristina O. Kvashnina:** Writing – review & editing, Validation, Methodology, Investigation. **Nina Huittinen:** Writing – review & editing, Project administration, Funding acquisition. **Lars Peters:** Writing – review & editing, Supervision, Funding acquisition, Conceptualization.

Declaration of competing interest

The authors declare that they have no known competing financial interests or personal relationships that could have appeared to influence the work reported in this paper.

Data availability

The raw data from powder XRD and in-situ HERFD-XANES measurements have been made available on Zenodo. The corresponding DOI's can be found in the references.

Appendix A. Supplementary data

Supplementary material related to this article can be found online at https://doi.org/10.1016/j.jssc.2024.124784.

References

[1] IAEA, Nuclear power reactors in the world, in: Reference Data Series, (no. 2) International Atomic Energy Agency, Vienna, 2023.

[2] W. Lee, M. Ojovan, M. Stennett, N. Hyatt, Immobilisation of radioactive waste in glasses, glass composite materials and ceramics, Adv. Appl. Ceram. 105 (1) (2006) 3–12, http://dx.doi.org/10.1179/174367606X81669.

[3] C. Jantzen, Development of glass matrices for high level radioactive wastes, in: Handbook of Advanced Radioactive Waste Conditioning Technologies, Elsevier, 2011, pp. 230–292, http://dx.doi.org/10.1533/9780857090959.2.230.

[4] W.J. Weber, R.C. Ewing, C.A. Angell, G.W. Arnold, A.N. Cormack, J.M. Delaye, D.L. Griscom, L.W. Hobbs, A. Navrotsky, D.L. Price, et al., Radiation effects in glasses used for immobilization of high-level waste and plutonium disposition, J. Mater. Res. 12 (8) (1997) 1948–1978, http://dx.doi.org/10.1557/JMR.1997.0266.

[5] W.J. Weber, A. Navrotsky, S. Stefanovsky, E.R. Vance, E. Vernaz, Materials science of high-level nuclear waste immobilization, MRS Bull. 34 (1) (2009) 46–53, http://dx.doi.org/10.1557/mrs2009.12.

[6] M.I. Ojovan, W.E. Lee, S.N. Kalmykov, Immobilisation of radioactive wastes in glass, in: An Introduction to Nuclear Waste Immobilisation, Elsevier, 2019, pp. 319–368.

[7] B.K. Singh, M.A. Hafeez, H. Kim, S. Hong, J. Kang, W. Um, Inorganic waste forms for efficient immobilization of radionuclides, ACS ES&T Eng. 1 (8) (2021) 1149–1170, http://dx.doi.org/10.1021/acsestengg.1c00184.

[8] I. Donald, B. Metcalfe, R. Taylor, The immobilization of high level radioactive wastes using ceramics and glasses, J. Mater. Sci. 32 (22) (1997) 5851–5887, http://dx.doi.org/10.1023/A:1018646507438.

[9] L. Hatch, Ultimate disposal of radioactive wastes, Am. Sci. 41 (3) (1953) 410–421.

[10] H. Schlenz, S. Neumeier, A. Hirsch, L. Peters, G. Roth, 9. Phosphates as safe containers for radionuclides, in: Highlights in Applied Mineralogy, De Gruyter, 2017, pp. 171–196, http://dx.doi.org/10.1515/9783110497342.

[11] G.R. Watt, High-thorium monazite-(Ce) formed during disequilibrium melting of metapelites under granulite-facies conditions, Mineral. Mag. 59 (397) (1995) 735–743, http://dx.doi.org/10.1180/minmag.1995.059.397.14.

[12] W.C. Overstreet, The geologic occurrence of monazite, Technical Report, US Geological Survey, 1967, http://dx.doi.org/10.3133/pp530.

[13] C. Gramaccioli, T. Segalstad, A uranium- and thorium-rich monazite from a south-alpine pegmatite at Piona, Italy, Am. Mineral. 63 (7–8) (1978) 757–761.

[14] N. Dacheux, N. Clavier, R. Podor, Monazite as a promising long-term radioactive waste matrix: Benefits of high-structural flexibility and chemical durability, Am. Mineral. 98 (5–6) (2013) 833–847, http://dx.doi.org/10.2138/am.2013.4307.

[15] L. Nasdala, S. Akhmadaliev, B.E. Burakov, C. Chanmuang N, R. Škoda, The absence of metamictisation in natural monazite, Sci. Rep. 10 (1) (2020) 1–9, http://dx.doi.org/10.1038/s41598-020-71451-7.

[16] A. Meldrum, L.A. Boatner, R.C. Ewing, Displacive radiation effects in the monazite- and zircon-structure orthophosphates, Phys. Rev. B 56 (1997) 13805–13814, http://dx.doi.org/10.1103/PhysRevB.56.13805.

[17] D. Mullica, W. Milligan, D.A. Grossie, G. Beall, L. Boatner, Ninefold coordination LaPO4: Pentagonal interpenetrating tetrahedral polyhedron, Inorg. Chim. Acta 95 (4) (1984) 231–236, http://dx.doi.org/10.1016/S0020-1693(00)87472-1.

[18] D. Mullica, C. Lok, D.A. Grossie, A new nine-coordination system: pentagonal interpenetrating tetrahedral polyhedron, J. Solid State Chem. 63 (3) (1986) 452–454, http://dx.doi.org/10.1016/0022-4596(86)90204-5.

[19] C.W. Bjorklund, The preparation of PuP2O7 and PuPO4, J. Am. Chem. Soc. 79 (24) (1957) 6347–6350.

[20] C. Keller, K. Walter, Darstellung, Gitterkonstanten und chemische Eigenschaften einiger ternärer Oxide des Plutoniums, Americiums und Curiums vom Typ MeIIIXVO4, J. Inorg. Nucl. Chem. 27 (6) (1965) 1253–1260, http://dx.doi.org/10.1016/0022-1902(65)80087-2.

[21] R. Haire, H. Hellwege, D. Hobart, J. Young, Syntheses, lattice parameters and solid state absorption spectra of the first five transplutonium orthophosphates, J. Less-Common Met. 93 (2) (1983) 358–359.

[22] D. Hobart, G. Begun, R. Haire, H. Hellwege, Raman spectra of the transplutonium orthophosphates and trimetaphosphates, J. Raman Spectrosc. 14 (1) (1983) 59–62, http://dx.doi.org/10.1002/jrs.1250140114.

[23] R. De Biasi, A. Fernandes, J. Oliveira, Cell volumes of LaPO4–CePO4 solid solutions, J. Appl. Crystallogr. 20 (4) (1987) 319–320, http://dx.doi.org/10.1107/S0021889887086606.

[24] O. Terra, N. Clavier, N. Dacheux, R. Podor, Preparation and characterization of lanthanum–gadolinium monazites as ceramics for radioactive waste storage, New J. Chem. 27 (6) (2003) 957–967, http://dx.doi.org/10.1039/B212805P.

[25] N. Kitamura, K. Amezawa, Y. Tomii, N. Yamamoto, T. Hanada, Protonic conduction in Sr-doped (La1-xSmx)PO4, Solid State Ion. 175 (1–4) (2004) 563–567, http://dx.doi.org/10.1016/j.ssi.2004.02.077.

[26] K. Popa, R. Konings, T. Geisler, High-temperature calorimetry of (La1- xlnx) PO4 solid solutions, J. Chem. Thermodyn. 39 (2) (2007) 236–239, http://dx.doi.org/10.1016/j.jct.2006.07.010.

[27] P. Yang, Z. Quan, C. Li, Z. Hou, W. Wang, J. Lin, Solvothermal synthesis and luminescent properties of monodisperse LaPO4: Ln (Ln=Eu3+, Ce3+, Tb3+) particles, J. Solid State Chem. 182 (5) (2009) 1045–1054, http://dx.doi.org/10.1016/j.jssc.2009.01.024.

[28] Z. Hou, L. Wang, H. Lian, R. Chai, C. Zhang, Z. Cheng, J. Lin, Preparation and luminescence properties of Ce3+ and/or Tb3+ doped LaPO4 nanofibers and microbelts by electrospinning, J. Solid State Chem. 182 (4) (2009) 698–708, http://dx.doi.org/10.1016/j.jssc.2008.12.021.

[29] N. Yaiphaba, R. Ningthoujam, N.S. Singh, R. Vatsa, N.R. Singh, Probing of inversion symmetry site in Eu3+-doped GdPO4 by luminescence study: Concentration and annealing effect, J. Lumin. 130 (1) (2010) 174–180, http://dx.doi.org/10.1016/j.jlumin.2009.08.008.

[30] A. Hirsch, P. Kegler, I. Alencar, J. Ruiz-Fuertes, A. Shelyug, L. Peters, C. Schreinemachers, A. Neumann, S. Neumeier, H.-P. Liermann, et al., Structural, vibrational, and thermochemical properties of the monazite-type solid solution La1–xPrxPO4, J. Solid State Chem. 245 (2017) 82–88, http://dx.doi.org/10.1016/j.jssc.2016.09.032.

[31] A. Tabuteau, J. Livet, C. Musikas, et al., Monazite-like phases containing transuranium elements (neptunium and plutonium), J. Mater. Sci. Lett. 7 (12) (1988) 1315–1317, http://dx.doi.org/10.1007/BF00719969.

[32] J.M. Montel, J.L. Devidal, D. Avignant, X-ray diffraction study of brabantite–monazite solid solutions, Chem. Geol. 191 (1–3) (2002) 89–104, http://dx.doi.org/10.1016/S0009-2541(02)00150-X.

[33] O. Terra, N. Dacheux, N. Clavier, R. Podor, F. Audubert, Preparation of optimized uranium and thorium bearing brabantite or monazite/brabantite solid solutions, J. Am. Ceram. Soc. 91 (11) (2008) 3673–3682, http://dx.doi.org/10.1111/j.1551-2916.2008.02678.x.

[34] P.E. Raison, R. Jardin, D. Bouëxière, R.J. Konings, T. Geisler, C.C. Pavel, J. Rebizant, K. Popa, Structural investigation of the synthetic CaAn (PO4) 2 (An=Th and Np) cheralite-like phosphates, Phys. Chem. Miner. 35 (10) (2008) 603–609, http://dx.doi.org/10.1007/s00269-008-0252-4.

[35] D. Bregiroux, O. Terra, F. Audubert, N. Dacheux, V. Serin, R. Podor, D. Bernache-Assollant, Solid-state synthesis of monazite-type compounds containing tetravalent elements, Inorg. Chem. 46 (24) (2007) 10372–10382, http://dx.doi.org/10.1021/ic7012123.

[36] K. Popa, D. Bregiroux, R.J. Konings, T. Gouder, A.F. Popa, T. Geisler, P.E. Raison, The chemistry of the phosphates of barium and tetravalent cations in the 1: 1 stoichiometry, J. Solid State Chem. 180 (8) (2007) 2346–2355, http://dx.doi.org/10.1016/j.jssc.2007.06.006.

[37] D. Bregiroux, R. Belin, P. Valenza, F. Audubert, D. Bernache-Assollant, Plutonium and americium monazite materials: Solid state synthesis and X-ray diffraction study, J. Nucl. Mater. 366 (1–2) (2007) 52–57, http://dx.doi.org/10.1016/j.jnucmat.2006.12.042.

[38] A. Orlova, D. Kitaev, N. Kazantsev, S. Samoilov, V. Kurazhkovskaya, E. Vopilina, Double phosphates of Ce (IV) and some mono-and divalent elements: synthesis and crystal structure, Radiochemistry 44 (4) (2002) 326–331, http://dx.doi.org/10.1023/A:1020656407183.

[39] D. Kitaev, Y.F. Volkov, A. Orlova, Orthophosphates of tetravalent Ce, Th, U, Np, and Pu with the monazite structure, Radiochemistry 46 (2004) 211–217, http://dx.doi.org/10.1023/B:RACH.0000031674.74780.a8.

[40] P.A. Bingham, R.J. Hand, M.C. Stennett, N.C. Hyatt, M.T. Harrison, The use of surrogates in waste immobilization studies: A case study of plutonium, MRS Online Proc. Libr. (OPL) 1107 (2008) http://dx.doi.org/10.1557/PROC-1107-421.

[41] T.P. Gompa, A. Ramanathan, N.T. Rice, H.S. La Pierre, The chemical and physical properties of tetravalent lanthanides: Pr, Nd, Tb, and Dy, Dalton Trans. 49 (45) (2020) 15945–15987, http://dx.doi.org/10.1039/D0DT01400A.

[42] R.D. Shannon, Revised effective ionic radii and systematic studies of interatomic distances in halides and chalcogenides, Acta Crystallogr. A 32 (5) (1976) 751–767, http://dx.doi.org/10.1107/S0567739476001551.

[43] C. Lopez, X. Deschanels, J. Bart, J. Boubals, C. Den Auwer, E. Simoni, Solubility of actinide surrogates in nuclear glasses, J. Nucl. Mater. 312 (1) (2003) 76–80, http://dx.doi.org/10.1016/S0022-3115(02)01549-0.

[44] B. Metcalfe, S. Fong, L. Gerrard, I. Donald, E. Welch, M. Stennett, N. Hyatt, The relative merits of oxides of hafnium, cerium and thorium as surrogates for plutonium oxide in calcium phosphate ceramics, MRS Online Proc. Libr. (OPL) 1193 (2009) http://dx.doi.org/10.1557/PROC-1193-79.

[45] J.M. Heuser, S. Neumeier, L. Peters, H. Schlenz, D. Bosbach, G. Deissmann, Structural characterisation of metastable Tb- and Dy-monazites, J. Solid State Chem. 273 (2019) 45–52, http://dx.doi.org/10.1016/j.jssc.2019.02.028.

[46] H.M. Rietveld, Line profiles of neutron powder-diffraction peaks for structure refinement, Acta Crystallogr. 22 (1) (1967) 151–152, http://dx.doi.org/10.1107/S0365110X67000234.

[47] R.W. Cheary, A. Coelho, A fundamental parameters approach to X-ray line-profile fitting, J. Appl. Crystallogr. 25 (1992) 109–121, http://dx.doi.org/10.1107/S0021889891010804.

[48] A. Hirsch, P. Kegler, I. Alencar, J. Ruiz-Fuertes, A. Shelyug, L. Peters, C. Schreinemachers, A. Neumann, S. Neumeier, H.P. Liermann, A. Navrotsky, G. Roth, Structural, vibrational, and thermochemical properties of the monazite-type solid solution La1–xPrxPO4, J. Solid State Chem. 245 (2017) 82–88, http://dx.doi.org/10.1016/j.jssc.2016.09.032, URL https://www.sciencedirect.com/science/article/pii/S0022459616303875.

[49] H.G. Scott, The estimation of standard deviations in powder diffraction Rietveld refinements, J. Appl. Crystallogr. 16 (2) (1983) 159–163, http://dx.doi.org/10.1107/S0021889883010195.

[50] J.F. Bérar, P. Lelann, E.s.d.'s and estimated probable error obtained in Rietveld refinements with local correlations, J. Appl. Crystallogr. 24 (1) (1991) 1–5, http://dx.doi.org/10.1107/S0021889890008391.

[51] T. Lender, PXRD Data of the La1-xCex/2Cax/2 Solid Solution Produced by Solid State and Co-Precipitation Synthesis, Zenodo, 2023, http://dx.doi.org/10.5281/zenodo.10610331.

[52] E. Jarosewich, L. Boatner, Rare-earth element reference samples for electron microprobe analysis, Geostand. Newsl. 15 (2) (1991) 397–399, http://dx.doi.org/10.1111/j.1751-908X.1991.tb00115.x.

[53] J.J. Donovan, J.M. Hanchar, P.M. Picolli, M.D. Schrier, L.A. Boatner, E. Jarosewich, A re-examination of the rare-earth-element orthophosphate standards in use for electron-microprobe analysis, Can. Mineral. 41 (1) (2003) 221–232, http://dx.doi.org/10.2113/gscanmin.41.1.221.

[54] A.C. Scheinost, J. Claussner, J. Exner, M. Feig, S. Findeisen, C. Hennig, K.O. Kvashnina, D. Naudet, D. Prieur, A. Rossberg, et al., ROBL-II at ESRF: a synchrotron toolbox for actinide research, J. Synchrotron Radiat. 28 (1) (2021) 333–349, http://dx.doi.org/10.1107/S1600577520014265.

[55] K.O. Kvashnina, A.C. Scheinost, A Johann-type X-ray emission spectrometer at the Rossendorf beamline, J. Synchrotron Radiat. 23 (3) (2016) 836–841, http://dx.doi.org/10.1107/S1600577516004483.

[56] B. Ravel, M. Newville, ATHENA, ARTEMIS, hephaestUS: data analysis for X-ray absorption spectroscopy using IFEFFIT, J. Synchrotron Radiat. 12 (4) (2005) 537–541, http://dx.doi.org/10.1107/S0909049505012719.

[57] A. Rossberg, T. Reich, G. Bernhard, Complexation of uranium (vi) with protocatechuic acid–application of iterative transformation factor analysis to exafs spectroscopy, Anal. Bioanal. Chem. 376 (2003) 631–638, http://dx.doi.org/10.1007/s00216-003-1963-5.

[58] T. Lender, E. Bazarkina, K. Kvashnina, In-situ XANES Data for the calcination of Ca(II)/Ce(IV)-doped LaPO4 Monazite, Zenodo, 2023, http://dx.doi.org/10.5281/zenodo.10606662.

[59] D. Bregiroux, F. Audubert, D. Bernache-Assollant, Study of Tetravalent Cerium Incorporation in the Monazite Structure, Technical Report, U.S. Department of Energy, 2004.

[60] A. Hirsch, Monazite Solid Solutions - Characterisation of Structural, Thermal and Physical Properties (Ph.D. thesis), RWTH Aachen University, Aachen, 2018, http://dx.doi.org/10.18154/RWTH-2018-225331, 1 Online–Ressource (xviii, 169 Seiten) : Illustrationen, URL https://publications.rwth-aachen.de/record/726942.

[61] D. Qin, A. Mesbah, N. Clavier, S. Szenknect, N. Dacheux, From th-rhabdophane to monazite-cheralite solid solutions: Thermal behavior of Nd1–2 x th x Ca x PO4· n H2O (x=0–0.15), Cryst. Growth Des. 19 (5) (2019) 2794–2801.

[62] X. Zhao, W. Wang, Y. Teng, Y. Li, X. Ma, Y. Liu, R. Ahuja, W. Luo, Z. Zhang, Incorporation of Th4+ and Sr2+ into rhabdophane/monazite by wet chemistry: Structure and phase stability, Inorg. Chem. 62 (38) (2023) 15605–15615.

[63] T. Lender, L.B.F. dos Santos, R. Gericke, N. Huittinen, L. Peters, Optimisation of synthesis procedures and structural investigation of monazite-cheralite solid solutions, MRS Adv. (2024) 1–6.

[64] A. Matraszek, I. Szczygieá, L. Macalik, J. Hanuza, Mechanochemical synthesis of cerium orthophosphate, J. Rare Earths 27 (4) (2009) 598–602, http://dx.doi.org/10.1016/S1002-0721(08)60296-3.

[65] A. Mesbah, N. Clavier, E. Elkaim, C. Gausse, I.B. Kacem, S. Szenknect, N. Dacheux, Monoclinic form of the rhabdophane compounds: REEPO4*0.667H2O, Cryst. Growth Des. 14 (10) (2014) 5090–5098, http://dx.doi.org/10.1021/cg500707b.

[66] S. Lucas, E. Champion, D. Bernache-Assollant, G. Leroy, Rare earth phosphate powders RePO4· nH2O (Re=La, Ce or Y) II. thermal behavior, J. Solid State Chem. 177 (4–5) (2004) 1312–1320, http://dx.doi.org/10.1016/j.jssc.2003.11.004.

[67] N. Clavier, R. Podor, N. Dacheux, Crystal chemistry of the monazite structure, J. Eur. Ceram. Soc. 31 (6) (2011) 941–976, http://dx.doi.org/10.1016/j.jeurceramsoc.2010.12.019.

[68] K. Kvashnina, S. Butorin, P. Glatzel, Direct study of the f-electron configuration in lanthanide systems, J. Anal. At. Spectrom. 26 (2011) 1265–1272, http://dx.doi.org/10.1039/C0JA00142B.

[69] P.E. Raison, S. Heathman, G. Wallez, C.E. Zvoriste, D. Bykov, G. Ménard, E. Suard, K. Popa, N. Dacheux, R.J. Konings, et al., Structure and nuclear density distribution in the cheralite—CaTh (PO 4) 2: studies of its behaviour under high pressure (36 GPa), Phys. Chem. Miner. 39 (2012) 685–692.

[70] G. Gasperi, L. Amidani, F. Benedetti, F. Boscherini, P. Glatzel, S. Valeri, P. Luches, Electronic properties of epitaxial cerium oxide films during controlled reduction and oxidation studied by resonant inelastic X-ray scattering, Phys. Chem. Chem. Phys. 18 (30) (2016) 20511–20517.

[71] E. Piskorska-Hommel, M. Winiarski, M. Kurnatowska, The low temperature reducibility of Ce4+ ions in Ce0.7Yb0.2Pd0.1O2-δ: in situ XANES study, Mater. Chem. Phys. 257 (2021) 123852, http://dx.doi.org/10.1016/j.matchemphys.2020.123852, URL https://www.sciencedirect.com/science/article/pii/S0254058420312116.

[72] L.M. Morgan, D. Loche, A. Corrias, S. Hayama, G. Mountjoy, Using ex situ and in situ HERFD-XANES to reveal the superior oxidation and reduction cycling of ceria nanocubes dispersed in silica aerogel, J. Phys. Chem. C 127 (39) (2023) 19554–19562.

[73] R.C. Weast, M.J. Astle, CRC Handbook of Chemistry and Physics, sixty ed., in: 100 Key Points, CRC Press Inc., 1980.

[74] C. Bamberger, R. Haire, H. Hellwege, G. Begun, Synthesis and characterization of crystalline phosphates of plutonium (III) and plutonium (IV), J. Less Common Met. 97 (1984) 349–356, http://dx.doi.org/10.1016/0022-5088(84)90040-7.